Numerical Heat Transfer, Part B, 40: 199–228, 2001

1040-7790/01 $12.00 + .00

A NEW BENCHMARK QUALITY SOLUTION FOR THE BUOYANCY-DRIVEN CAVITY BY DISCRETE SINGULAR CONVOLUTION

D. C. Wan, B. S. V. Patnaik, and G. W. Wei
Department of Computational Science, National University of Singapore, Republic of Singapore

This article introduces a high-accuracy discrete singular convolution (DSC) for the numerical simulation of coupled convective heat transfer problems. The problem of a buoyancy-driven cavity is solved by two completely independent numerical procedures. One is a quasi-wavelet-based DSC approach, which uses the regularized Shannon's kernel, while the other is a standard form of the Galerkin finite-element method. The integration of the Navier–Stokes and energy equations is performed by employing velocity correction-based schemes. The entire laminar natural convection range of $10^3 \leq \mathbf{Ra} \leq 10^8$ ***is numerically simulated by both schemes. The reliability and robustness of the present DSC approach is extensively tested and validated by means of grid sensitivity and convergence studies. As a result, a set of new benchmark quality data is presented. The study emphasizes quantitative, rather than qualitative comparisons.***

I. INTRODUCTION

Convection by natural means is crucial to flows, in both nature and technology. There are a variety of real-world applications of natural convection, such as thermal insulation, cooling of electronic equipment, solar energy devices, nuclear reactors, heat-recovery systems, room ventilation, crystal growth in liquids, etc. The fluid flow and heat transfer behavior of such systems can be predicted by the mass, momentum, and energy conservation equations with appropriate boundary conditions. The fast-emerging branch of computational fluid dynamics (CFD) facilitates the numerical simulation of fluid flow and heat transfer features. A comprehensive analysis of the fluid flow and heat transfer patterns in fundamentally simple geometries, such as the buoyancy-driven square cavity, is a necessary precursor to the evolution of better designs for more complex industrial applications.

Jones [1] has proposed the problem of a buoyancy-driven cavity as a suitable vehicle for testing and validation of computer codes for thermal problems. The simplicity of the geometry and the clarity in boundary conditions render this problem

Received 8 December 2000; accepted 1 March 2001.
This work was supported by the National University of Singapore and the National Science and Technology Board of the Republic of Singapore.
Address correspondence to Dr. G. W. Wei, Department of Computational Science, National University of Singapore, Block S 17, Level 7, 3 Science Drive, Singapore 117543. E-mail: cscweigw@nus.edu.sg

NOMENCLATURE

B	frequency bound
C	Courant number
E	error
g	acceleration due to gravity
Gr	Grashof number ($= g\beta\Delta\theta L_{\text{ref}}^3/\nu^2$)
L_{ref}	reference length dimension (either width or height)
L^2	error norm
Nu	Nusselt number
$\overline{\text{Nu}}$	average Nusselt number
p	nondimensional pressure ($= \bar{p}L_{\text{ref}}^2/\rho\alpha^2$)
$\bar{p}$	dimensional pressure
Pe_c	cell Peclet number ($= u\Delta x/\nu$)
Pr	Prandtl number ($= \nu/\alpha$)
r	ratio of σ over Δ
Ra	Rayleigh number ($= g\beta\Delta\theta L_{\text{ref}}^3/\nu\alpha$)
$R_\sigma(x)$	delta regularizer
$\bar{t}$	dimensional time
t	nondimensional time ($= \bar{t}\alpha/L_{\text{ref}}^2$)
u	nondimensional horizontal velocity ($= \bar{u}L_{\text{ref}}/\alpha$)
$\bar{u}$	dimensional horizontal velocity
U	nondimensional velocity vector (u, v)
v	nondimensional vertical velocity ($= \bar{v}L_{\text{ref}}/\alpha$)
$\bar{v}$	dimensional vertical velocity
W	bandwidth of support on one side of the grid point
$\bar{x}$	dimensional horizontal coordinate
x	nondimensional horizontal coordinate ($= \bar{x}/L_{\text{ref}}$)
x_k	discrete sampling points around the point x
y	nondimensional vertical coordinate ($= \bar{y}/L_{\text{ref}}$)
$\bar{y}$	dimensional vertical coordinate
α	thermal diffusivity of the fluid
$\alpha_1, \alpha_2, \alpha_3$	constants used in the Runge–Kutta scheme [Eqs. (33), (34), (35)]
$\beta_1, \beta_2, \beta_3$	constants used in the Runge–Kutta scheme [Eqs. (33), (34), (35)]
Δ	grid spacing, incremental value
$\delta_\Delta(x), \delta_{\Delta,\sigma}(x)$	convolution kernels
ϵ	a small parameter
η	variable of interest
θ	nondimensional temperature [$= (\bar{\theta} - \theta_C)/(\theta_H - \theta_C)$]
ν	kinematic viscosity
ρ	density
σ	width of the Gaussian envelope
ϕ	potential function
ω	relaxation parameter
$\bar{\theta}$	dimensional temperature
∇	gradient

Subscripts

C	cold wall
H	hot wall
i,j	indices in the horizontal and vertical direction, respectively

Superscripts

$*$	intermediate field value
l,n	iteration labels
q	order of the derivative

more appealing for new computational algorithms. In the early 1980s, this problem was solved by a number of different groups and their results were extensively summarized in the standard reference by de Vahl Davis and Jones [2]. De Vahl Davis [3] used forward difference for the temporal discretization and second-order central difference for the spatial discretization, to solve the stream function-vorticity form of the equations. The resulting algebraic equations were solved by an alternating-direction implicit (ADI) algorithm. Although the solution obtained was among the best of those days, the data presented were limited to a Rayleigh number (Ra) of 10^6. It is pertinent to quote Professor de Vahl Davis from his seminal article [3]:

> It is hoped that it will lead to further contributions to the search for efficient and high accuracy methods for problems of this type.

Even after nearly two decades, this statement remains sacrosanct, despite the phenomenal progress in numerical methods. A variety of computational algorithms has

been tested on this problem and the vast amount of literature is a testimony to this [1–10]. For example, Hortmann et al. [4] have employed a finite-volume-based multigrid technique for the simulation of a buoyancy-driven cavity. Ramaswamy et al. [8] have investigated the performance of two explicit and one semi-implicit projection-based schemes. They have concluded that the semi-implicit scheme always outperforms the two explicit schemes considered by them. In their numerical investigations, a variety of benchmark problems were solved, including the buoyancy-driven cavity. Shu and Xue [9] employed a global method of generalized differential quadrature (GDQ) for solving the stream function-vorticity form of the Navier-Stokes (N-S) equations. Massarotti et al. [5] used a semi-implicit form of the characteristic-based split scheme (CBS) with equal-order interpolation functions for all the variables. Manzari et al. [7] developed an artificial diffusion-based algorithm for 3-D compressible turbulent flow problems. This was later extended to 2-D laminar heat transfer problems. The basic idea of Manzari [6, 7] involves modification of continuity equation by employing the concept of artificial compressibility. Recently, Mayne et al. [10] employed an *h*-adaptive finite-element method to ensure a very accurate solution for the thermal cavity problem. Despite so much effort on this problem, there still exist some variations and discrepancies in the available literature (see the detailed discussion in Section III). Inherently, numerical results are approximations. Their accuracy and reliability depends vitally on the underlying computational method and the numerical scheme. Hence, further advances in computational methodology are crucial to the thermal cavity problem as well as other heat transfer problems.

A variety of computational methods are available in the literature. In a broad sense they can be classified into global and local methods. Global methods approximate a differentiation at a point by all grid points in the computational domain and can be highly accurate. Spectral methods, pseudo-spectral methods, fast Fourier transforms, and differential quadrature come under this category. For example, spectral methods converge exponentially with mesh refinement for approximating an analytical function and thus have the potential to be used in high-precision and demanding large-scale computations. Many global approaches have been successfully applied to the study of fluid flow and heat transfer in simple geometries, such as cavities, channels, ducts, diffusers, etc. However, global methods have limited capability in handling irregular geometries and more complex boundary conditions. Indeed, local methods, such as finite differences, finite-elements, finite strips, and finite volumes, are the most popular approaches for solving engineering problems. Local methods utilize information from the nearest neighboring grid points to approximate the differentiation at a point and thus are much more flexible. However, local methods converge slowly with respect to mesh refinement and are not cost-effective for achieving high precision. Hence, there is a strong demand for a scheme which can exploit the advantages of both methods. To this end, a high-accuracy quasi-wavelet-based approach, the discrete singular convolution (DSC), was proposed [13]. This method is a promising approach for the numerical realization of singular convolutions [14, 15]. Mathematical foundation for this algorithm stems from the theory of distributions (or generalized functions). Sequence of approximations to the singular kernels of Hilbert type, Abel type, and delta type can be constructed. Numerical solution to differential equations are formulated via singular kernels of delta type.

The DSC approach exhibits global methods' accuracy for integration and local methods' flexibility in handling irregular geometries and complex boundary conditions, when suitable DSC kernels are chosen. Many DSC kernels, such as (regularized) Shannon's delta kernel, (regularized) Dirichlet kernel, (regularized) Lagrange kernel, and (regularized) de la Vallée Poussin kernel, are constructed for a number of applications, such as numerical solution of the Fokker–Planck equation [14, 15] and the Schrödinger equation [16]. The DSC algorithm was also utilized for waveguide model analysis, electromagnetic wave propagation [17], and structural (plate and beam) analysis [18–20] with excellent results. Most recently, the DSC algorithm was used to resolve a few numerically challenging problems. The integration of the (nonlinear) sine-Gordon equation [21] with the initial values close to a homoclinic orbit singularity is one such problem for which conventional local methods have encountered great difficulty and numerically induced chaos was reported [22]. Another complex problem that has been resolved by using the DSC algorithm is the integration of the (nonlinear) Cahn–Hilliard equation in a circular domain [23], which is challenging because of the fourth-order artificial singularity at the origin and complex phase-space geometry. DSC solution of *machine precision* to the Navier–Stokes equations with periodic boundary conditions for the Taylor problem was obtained with 33 grid points in each dimension [15, 18]. Recently, a DSC finite-subdomain method was proposed for the solution of incompressible viscous flows under complex geometries [24].

The objectives of the present study are the following: (1) To introduce the highly accurate quasi-wavelet-based discrete singular convolution [15, 18] for the numerical simulation of coupled convective heat transfer problems; (2) to present benchmark-quality data for the entire laminar natural-convection range of $10^3 \leq \mathrm{Ra} \leq 10^8$; and (3) to present a focused and elaborate study on the problem of the buoyancy-driven cavity, which also looks into some of the discrepancies observed in the literature. The high level of accuracy that could be achieved for the Taylor problem [15, 18] enhances the level of confidence and reliability for the simulation of the driven-cavity problem. The DSC code is extensively tested and further validated with a second-order-accurate finite-element-based Galerkin method, against the available numerical simulations of [3–10].

This article is organized into four sections. A description of the problem under investigation and the methods of solution by both DSC and FEM are presented in Section II. An elaborate and focused study on the results obtained for the buoyancy-driven cavity is presented in Section III. Conclusions are presented in Section IV.

II. THEORETICAL BACKGROUND AND METHODS OF SOLUTION

This section defines the buoyancy-driven cavity problem, including the governing partial differential equations (PDEs) and the boundary conditions. Two completely independent methods of solution, viz., a quasi-wavelet-based approach and a finite-element method, are employed to solve the problem under investigation. The theoretical framework behind the discrete singular convolution is elaborated. The method of solution for the integration of the Navier-Stokes and energy equations by the DSC and FEM is explained.

A. Problem Description

A differentially heated, closed square cavity is depicted in Figure 1, whose left and right vertical walls are maintained at θ_H and θ_C, respectively. The horizontal walls are adiabatic (insulated, and there is no transfer of heat through these walls). Fluid is assumed to be viscous, incompressible, Newtonian, and Boussinesq-approximated. The Newtonian assumption guarantees a linear relationship between the shear stress and the velocity gradient. The Boussinesq approximation means that the density differences are confined to the buoyancy term, without violating the assumption of incompressibility. It should be pointed out that there is an additional coupling term in the momentum equations, which indeed dictates the fluid motion within the cavity.

1. Governing equations. The governing PDEs are the coupled mass, momentum, and energy conservation equations, applicable for two dimensions. The equations are given as

$$\text{Continuity:} \qquad \frac{\partial u}{\partial x} + \frac{\partial v}{\partial y} = 0 \tag{1}$$

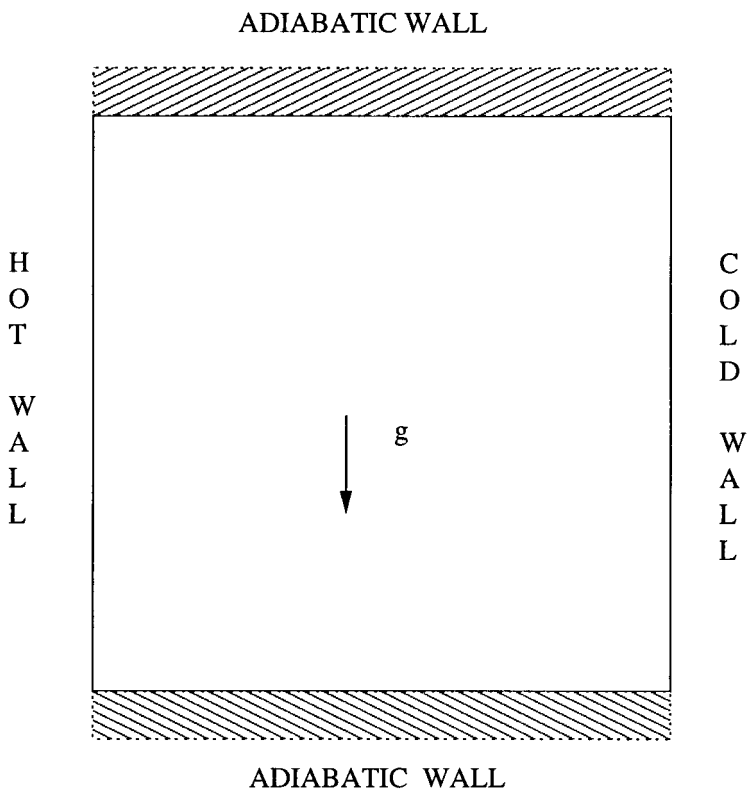

Figure 1. Flow domain of interest.

$$x \text{ momentum:} \qquad \frac{\partial u}{\partial t} + u\frac{\partial u}{\partial x} + v\frac{\partial u}{\partial y} = -\frac{\partial p}{\partial x} + \Pr\left(\frac{\partial^2 u}{\partial x^2} + \frac{\partial^2 u}{\partial y^2}\right) \tag{2}$$

$$y \text{ momentum:} \qquad \frac{\partial v}{\partial t} + u\frac{\partial v}{\partial x} + v\frac{\partial v}{\partial y} = -\frac{\partial p}{\partial y} + \Pr\left(\frac{\partial^2 v}{\partial x^2} + \frac{\partial^2 v}{\partial y^2}\right) + \mathrm{Ra}\,\Pr\,\theta \tag{3}$$

$$\text{Energy:} \qquad \frac{\partial \theta}{\partial t} + u\frac{\partial \theta}{\partial x} + v\frac{\partial \theta}{\partial y} = \frac{\partial^2 \theta}{\partial x^2} + \frac{\partial^2 \theta}{\partial y^2} \tag{4}$$

In the equations above, the following nondimensionalization was employed:

$$x = \frac{\bar{x}}{L_{\mathrm{ref}}} \qquad y = \frac{\bar{y}}{L_{\mathrm{ref}}} \qquad u = \frac{\bar{u}L_{\mathrm{ref}}}{\alpha} \qquad v = \frac{\bar{v}L_{\mathrm{ref}}}{\alpha} \qquad t = \frac{\bar{t}\alpha}{L_{\mathrm{ref}}^2} \tag{5}$$

$$p = \frac{\bar{p}L_{\mathrm{ref}}^2}{\rho\alpha^2} \qquad \theta = \frac{\bar{\theta} - \theta_C}{\theta_H - \theta_C} \qquad \mathrm{Ra} = \frac{g\beta\Delta\theta L_{\mathrm{ref}}^3}{\nu\alpha} \qquad \Pr = \frac{\nu}{\alpha} \tag{6}$$

In convection, density differences generate an additional force (popularly known as the buoyancy force), which competes with the inertial and viscous forces. The ratio of buoyancy to viscous forces is given by the parameter Grashof number (Gr), which controls natural convection. On the other hand, the ratio of momentum to thermal diffusivity, known as Prandtl number (Pr), governs the temperature field and its relationship with the fluid flow characteristics. Rayleigh number (Ra), which is the parameter of interest, is the product of these two dimensionless groups.

2. Boundary conditions. No-slip velocity boundary condition ($u = v = 0.0$) is applied on all four walls of the square cavity. For temperature, Dirichlet boundary conditions of $\theta_H = 1.0$ and $\theta_C = 0.0$ are enforced on the left and right vertical walls, respectively. As there is no transfer of heat through the horizontal walls, a Neumann boundary condition ($\partial\theta/\partial y = 0.0$), is applied.

3. The laminar-flow region. According to Incropera and Dewitt [11], the laminar natural convection at a local Rayleigh number larger than 10^9 may be promoted to turbulent transition in the vertical boundary layer. Undoubtedly, the transition from laminar to turbulence causes an increase in convective heat transfer on the surface of the wall. In their direct numerical simulation (DNS) of air flow in a square cavity, Paolucci and Chenoweth [12] detected the existence of a critical Rayleigh number between 10^8 and 2×10^8, where the flow undergoes a Hopf bifurcation into a periodic unsteady flow. Therefore, we confine the present simulations to the lower limit of this Rayleigh number, which is 10^8. Beyond this value, a Reynolds averaged form of the Navier–Stokes and energy equations would have to be employed together with a workable turbulence model.

B. Discrete Singular Convolution

1. Approximation of singular convolution. For the sake of clarity and integrity in presentation, the section begins with a brief description of the discrete

singular convolution (DSC) algorithm. Elaborate details are available in previous studies [14, 15]. The DSC algorithm concerns with the computer realization of the mathematical distributions. Distributions are not well defined in the usual sense and may not have any value. Particular examples are kernels of the Hilbert type and Abel type. These singular kernels are of crucial importance to a number of fields, such as Radon transform, analytical function theory, linear response theory, etc. For data (surface) interpolation and solving partial differential equations, singular kernels of delta type are useful. In the DSC algorithm, the function $f(x)$ and its derivatives with respect to the coordinate at a grid point x are approximated by a linear sum of discrete values $\{f(x_k)\}$ in the narrow bandwidth $[x - x_W, x + x_W]$. This can be expressed as

$$f^{(q)}(x) \approx \sum_{k=-W}^{W} \delta_{\Delta,\sigma}^{(q)}(x - x_k) f(x_k) \tag{7}$$

where superscript q $(q = 0, 1, 2, \ldots)$ denotes the qth-order derivative with respect to x. The $\{x_k\}$ refers to a set of discrete sampling points centered around the point x. Here σ is a regularization parameter, Δ is the grid spacing, and $2W + 1$ is the total computational bandwidth, which is usually much smaller than the computational domain.

In Eq. (7), $\delta_{\Delta,\sigma}(x)$ is a convolution kernel that approximates the delta distribution. For band-limited functions, the delta distribution can be replaced by a low-pass filter, hence, many wavelet scaling functions can be used as DSC convolution kernels. One interesting example is Shannon's wavelet scaling function,

$$\delta_{\Delta}(x) = \frac{\sin(\pi x/\Delta)}{\pi x/\Delta} \tag{8}$$

In fact, Shannon's wavelet scaling function forms a sampling basis for the Paley-Wiener reproducing kernel Hilbert space. Shannon's wavelet scaling is useful in solving eigenvalue problems with smoothly confined potentials [14] and for purely periodic boundary conditions [21]. However, for general computational problems, it is important to regularize Shannon's delta kernel,

$$\delta_{\Delta,\sigma}(x) = \delta_{\Delta}(x) R_{\sigma}(x) \tag{9}$$

where $R_{\sigma}(x)$ is a delta regularizer [13, 14], which can dramatically increase the regularity of Shannon's wavelet scaling function. An often-used delta regularizer is the Gaussian

$$R_{\sigma}(x) = \exp\left(-\frac{x^2}{2\sigma^2}\right) \qquad \sigma > 0 \tag{10}$$

where σ determines the width of the Gaussian envelop and can be varied in association with the grid spacing, i.e., $\sigma = r\Delta$. It should be pointed out that the use of appropriate regularizers can extend the domain of applicability of delta kernels to temporal distributions and even to exponentially growing functions [13].

The expression in Eq. (7) provides extremely high computational efficiency both on and off a grid. In fact, it can provide exact results when the sampling points are extended to a set of infinite points for certain band-limited L^2 functions. Qian and Wei [25] have given a mathematical estimation for the choice of W, r, and Δ. For example, if the L^2 error for approximating an L^2 function $f(x)$ is set to $10^{-\eta}$, the following relations would give the best accuracy:

$$r(\pi - B\Delta) > \sqrt{4.61\eta} \quad \text{and} \quad \frac{W}{r} > \sqrt{4.61\eta} \tag{11}$$

where $r = \sigma/\Delta$ and B is the frequency bound for the function of interest, $f(x)$. The first inequality states that for a given grid size Δ, a large r is required for approximating the high-frequency component of an L^2 function. The second inequality indicates that if one chooses the ratio $r = 3$, then the half-bandwidth $W \approx 30$ is good enough to achieve the highest accuracy in double-precision computations ($\eta = 15$). By appropriately choosing W, r, and Δ, the resulting approximation matrix for interpolation and solving the differential equations has a banded structure. This ensures that the DSC algorithm attains optimal accuracy and efficiency.

It should be pointed out that although regularized Shannon's delta kernel is used to illustrate the DSC approximation of the delta distribution here, there are a variety of other DSC kernels, such as (regularized) Dirichlet kernels, (regularized) Lagrange kernels, and (regularized) de la Vallée kernels, which perform equally well [14, 17, 21]. The grid used in Eq. (7) is uniform because only a single grid spacing is prescribed. In computations, Eq. (7) is very efficient since just one kernel is required for the whole computational domain $[a, b]$ for a given Δ and r. Thus, the kernel acquires the property of translational invariance. In order to maintain this property near a computational boundary, the functions $f(x_k)$ have to be located outside the computational domain $[a, b]$, where their values are usually undefined. Therefore, it is necessary to create fictitious domains outside the computational boundaries. For the DSC algorithm, function values in these fictitious domains are generated according to the boundary conditions and the physical behavior of the solution at the boundaries. For example, when Dirichlet boundary conditions are employed, $f(x_k)$ in the fictitious domain can be taken to be either $f(a)$ or $f(b)$; for a periodic boundary condition, $f(x_k)$ may be enforced by a periodic extension inside the computational domain $[a, b]$ to outside. Neumann boundary condition for $f(x_k)$ may be obtained by $f'(a)$ or $f'(b)$.

When the regularized Shannon's delta kernel is used, the detailed expressions for $\delta^{(0)}_{\Delta,\sigma}(x)$, $\delta^{(1)}_{\Delta,\sigma}(x)$, and $\delta^{(2)}_{\Delta,\sigma}(x)$ can be given analytically as

$$\delta^{(0)}_{\Delta,\sigma}(x) = \begin{cases} \dfrac{\sin(\pi x/\Delta)\exp(-x^2/2\sigma^2)}{\pi x/\Delta} & (x \neq 0) \\ 1 & (x = 0), \end{cases} \tag{12}$$

$$\delta^{(1)}_{\Delta,\sigma}(x) = \begin{cases} \dfrac{\cos(\pi x/\Delta)\exp(-x^2/2\sigma^2)}{x} - \dfrac{\sin(\pi x/\Delta)\exp(-x^2/2\sigma^2)}{\pi x^2/\Delta} \\ -\dfrac{\sin(\pi x/\Delta)\exp(-x^2/2\sigma^2)}{\pi\sigma^2/\Delta} & (x \neq 0) \\ 0 & (x = 0) \end{cases} \tag{13}$$

and

$$\delta^{(2)}_{\Delta,\sigma}(x) = \begin{cases} \dfrac{-(\pi/\Delta)\sin(\pi x/\Delta)\exp(-x^2/2\sigma^2)}{x} - 2\dfrac{\cos(\pi x/\Delta)\exp(-x^2/2\sigma^2)}{x^2} \\ -2\dfrac{\cos(\pi x/\Delta)\exp(-x^2/2\sigma^2)}{\sigma^2} + 2\dfrac{\sin(\pi x/\Delta)\exp(-x^2/2\sigma^2)}{\pi x^3/\Delta} \\ +\dfrac{\sin(\pi x/\Delta)\exp(-x^2/2\sigma^2)}{\pi\sigma^2 x/\Delta} + \dfrac{x\sin(\pi x/\Delta)\exp(-x^2/2\sigma^2)}{\pi\sigma^4/\Delta} & (x \neq 0) \\ -\dfrac{3+\pi^2\sigma^2/\Delta^2}{3\sigma^2} & (x = 0) \end{cases} \tag{14}$$

Once the parameter r is chosen, the coefficients $\delta^{(0)}_{\Delta,\sigma}(x)$, $\delta^{(1)}_{\Delta,\sigma}(x)$, and $\delta^{(2)}_{\Delta,\sigma}(x)$ depend only on the grid spacing Δ. Therefore, when the grid spacing is prescribed, the coefficients need to be computed only once and can be used during the whole computation. The good performance of the present DSC algorithm is due to the unique use of the DSC algorithm both for data interpolation and spatial discretization of the governing equations. Since the computational bandwidth is user-defined, the approximation accuracy is controllable in the present algorithm [15].

2. Solution methodology. For the convenience of presenting the method of solution, we define the following:

$$D(U) = \frac{\partial u}{\partial x} + \frac{\partial v}{\partial y} \tag{15}$$

$$L(U) = F(U) - \nabla p \tag{16}$$

$$F(U) = [f, g]^T \qquad U = [u, v]^T \qquad \nabla p = \left[\frac{\partial p}{\partial x}, \frac{\partial p}{\partial y}\right]^T \qquad M(\theta) = [m] \tag{17}$$

$$f = \mathrm{Pr}\left(\frac{\partial^2 u}{\partial x^2} + \frac{\partial^2 u}{\partial y^2}\right) - \left(u\frac{\partial u}{\partial x} + v\frac{\partial u}{\partial y}\right) \tag{18}$$

$$g = \mathrm{Pr}\left(\frac{\partial^2 zv}{\partial x^2} + \frac{\partial^2 v}{\partial y^2}\right) - \left(u\frac{\partial v}{\partial x} + v\frac{\partial v}{\partial y}\right) + \mathrm{Ra}\,\mathrm{Pr}\,\theta \tag{19}$$

$$m = \left(\frac{\partial^2 \theta}{\partial x^2} + \frac{\partial^2 \theta}{\partial y^2}\right) - \left(u\frac{\partial \theta}{\partial x} + v\frac{\partial \theta}{\partial y}\right) \tag{20}$$

Therefore, the system of Eqs. (1)–(4) can be simplified as follows:

$$D(U) = 0 \tag{21}$$

$$\frac{\partial U}{\partial t} = L(U) = F(U) - \nabla p \tag{22}$$

$$\frac{\partial \theta}{\partial t} = M(\theta) \tag{23}$$

A variety of fractional step approaches can be formulated by appropriately combining convective, viscous, and pressure terms of the momentum Eqs. (21)–(23).

When primitive variables are used in the governing PDEs, there is no direct link between the continuity and momentum equations. To bridge this gap, certain rearrangement of the momentum equations should be carried out, and thus the popular Poisson equation for pressure is formulated. In the simulation of Navier–Stokes equations, first an intermediate velocity is computed by omitting the pressure gradient, and later, it is corrected by including the same. This seminal idea was originally introduced by Chorin [26] in a finite-difference context. Since then, many special schemes have been designed and developed in this direction. For example, there is a family of implicit and semi-implicit pressure-correction methods such as the SIMPLE, consistent SIMPLE (SIMPLEC), and SIMPLER. Moreover, the artificial compressibility method, the marker and cell (MAC) method, the fractional-step projection method [26] and its many variants are also commonly used in the literature. In the present investigation, we adopt a fractional time-step and potential-function method (FTSPFM), which is a variant of the MAC method for solving the governing Eqs. (21)–(23). In this approach, an intermediate velocity field and a potential function are introduced and computed to update the velocity, pressure, and temperature in the domain.

3. Spatial discretization. In the present investigation a staggered grid system is employed. The momentum and energy equations in the horizontal direction is written at the point $(i+\frac{1}{2}, j)$, the momentum equation in the vertical direction is written at the point $(i, j+\frac{1}{2})$, and the pressure and temperature are given at point (i, j). The continuity equation is approximated at the point (i, j). All spatial derivatives in Eqs. (21)–(23) are discretized by using the DSC approach. A uniform grid in both x and y directions is employed. The discretized forms of Eqs. (15)–(20) can be expressed as follows:

$$D_h(U) = \sum_{k=-W}^{W} \delta^{(1)}_{\Delta,\sigma}(k\,\Delta x) u_{i+k,j} + \sum_{k=-W}^{W} \delta^{(1)}_{\Delta,\sigma}(k\,\Delta y) v_{i,j+k} \tag{24}$$

$$\nabla_h p = \left[\sum_{k=-W}^{W} \delta^{(1)}_{\Delta,\sigma}(k\,\Delta x) p_{i+k,j}, \sum_{k=-W}^{W} \delta^{(1)}_{\Delta,\sigma}(k\,\Delta y) p_{i,j+k} \right]^T \tag{25}$$

$$f_h = \mathrm{Pr}\left[\sum_{k=-W}^{W} \delta^{(2)}_{\Delta,\sigma}(k\,\Delta x) u_{i+\frac{1}{2}+k,j} + \sum_{k=-W}^{W} \delta^{(2)}_{\Delta,\sigma}(k\,\Delta y) u_{i+\frac{1}{2},j+k} \right] - \left[u_{i+\frac{1}{2},j} \sum_{k=-W}^{W} \delta^{(1)}_{\Delta,\sigma}(k\,\Delta x) u_{i+\frac{1}{2}+k,j} + v_{i+\frac{1}{2}j} \sum_{k=-W}^{W} \delta^{(1)}_{\Delta,\sigma}(k\,\Delta y) u_{i+\frac{1}{2},j+k} \right] \tag{26}$$

$$g_h = \mathrm{Pr}\left[\sum_{k=-W}^{W} \delta^{(2)}_{\Delta,\sigma}(k\,\Delta x) v_{i+k,j+\frac{1}{2}} + \sum_{k=-W}^{W} \delta^{(2)}_{\Delta,\sigma}(k\,\Delta y) v_{i,j+\frac{1}{2}+k} \right] - \left[u_{i,j+\frac{1}{2}} \sum_{k=-W}^{W} \delta^{(1)}_{\Delta,\sigma}(k\,\Delta x) v_{i+k,j+\frac{1}{2}} + v_{i,j+\frac{1}{2}} \sum_{k=-W}^{W} \delta^{(1)}_{\Delta,\sigma}(k\,\Delta y) v_{i,j+\frac{1}{2}+k} \right] + \mathrm{Ra}\,\mathrm{Pr}\,\theta_{i,j} \tag{27}$$

$$m_h = \left[\sum_{k=-W}^{W} \delta^{(2)}_{\Delta,\sigma}(k\,\Delta x)\theta_{i+k,j} + \sum_{k=-W}^{W} \delta^{(2)}_{\Delta,\sigma}(k\,\Delta y)\theta_{i,j+k} \right] - \left[u_{i,j} \sum_{k=-W}^{W} \delta^{(1)}_{\Delta,\sigma}(k\,\Delta x)\theta_{i+k,j} + v_{i,j} \sum_{k=-W}^{W} \delta^{(1)}_{\Delta,\sigma}(k\,\Delta y)\theta_{i,j+k} \right] \tag{28}$$

$$L_h(U) = F_h(U) - \nabla_h p$$
$$F_h(U) = [f_h, g_h]^T \qquad M_h(\theta) = [m_h] \tag{29}$$

where $\delta^{(1)}_{\Delta,\sigma}$ and $\delta^{(2)}_{\Delta,\sigma}$ are coefficients of the regularized Shannon's delta kernel, given in Eqs. (13) and (14), respectively. Here, the detailed labels (i, j) on U are omitted, and Δx and Δy denote the grid sizes in the x and y direction, respectively.

By substituting Eqs. (24)–(28) into Eqs. (21)–(23), the following semidiscretized approximations are obtained:

$$D_h(U) = 0 \tag{30}$$

$$\frac{dU}{dt} = L_h(U) = F_h(U) - \nabla_h p \tag{31}$$

$$\frac{d\theta}{dt} = M_h(\theta) \tag{32}$$

4. Temporal discretization. A Runge–Kutta scheme is used for temporal discretization. The scheme is of third-order accuracy in time and was used by many other authors [34, 35]. In this scheme, ordinary differential Eqs. (31)–(32) are formulated, which can be solved from the following:

$$U^{(1)} = \alpha_1 U^n + \beta_1\{\Delta t[F_h(U^n) - \nabla_h p^{(1)}]\} \tag{33}$$

$$U^{(2)} = \alpha_2 U^n + \beta_2\{U^{(1)} + \Delta t[F_h(U^{(1)}) - \nabla_h p^{(2)}]\} \tag{34}$$

$$U^{n+1} = \alpha_3 U^n + \beta_3\{U^{(2)} + \Delta t[F_h(U^{(2)}) - \nabla_h p^{n+1}]\} \tag{35}$$

$$\theta^{n+1} = \theta^n + \{\Delta t[M_h(\theta^n)]\} \tag{36}$$

where $(\alpha_1, \alpha_2, \alpha_3) = (1, \frac{3}{4}, \frac{1}{3})$ and $(\beta_1, \beta_2, \beta_3) = (1, \frac{1}{4}, \frac{2}{3})$. The $U^{(1)}$, $p^{(1)}$ and $U^{(2)}$, $p^{(2)}$, are their corresponding first and second step values for velocity and pressure, respectively.

5. Treatment for the pressure. Updating the pressure field requires special care. Therefore, a brief description of the treatment of pressure is given. At each step of the Runge–Kutta scheme, the FTSPFM [24] is adopted to solve Eqs. (30) and (31). To illustrate the present scheme, we consider the first step of the Runge–Kutta scheme. Assume that, at time t_n, the velocity U^n and pressure p^n are known, while $U^{(1)}$ and $p^{(1)}$ at the first step of the Runge–Kutta scheme are unknown. Let us introduce a first-step intermediate velocity field $U^{*(1)}$:

$$U^{*(1)} = \alpha_1 U^n + \beta_1 \{\Delta t[F_h(U^n) - \nabla_h p^n]\} \tag{37}$$

where $U^{*(1)}$ satisfies the same boundary condition as that for the physical velocity field U^{n+1} at time t_{n+1}.

Because Eq. (37) is explicit in terms of U^n and p^n, integration stability requires that the time increment satisfies the Courant-Friedrich-Lewy (CFL) condition,

$$\max(\Delta t) \leq \min\left\{\frac{4\,\mathrm{Pr}}{(|u| + |v|)^2}, \frac{\mathrm{Pr}[(\Delta x)^2 + (\Delta y)^2]}{4}\right\} \tag{38}$$

By subtracting Eq. (33) from Eq. (37), we have

$$U^{(1)} - U^{*(1)} = -\beta_1 \Delta t \nabla_h (p^{(1)} - p^n) \tag{39}$$

Since pressure is a scalar quantity, one can define a first-step potential function $\phi^{(1)}$ as

$$\phi^{(1)} = -\beta_1 \Delta t (p^{(1)} - p^n) \tag{40}$$

Hence, the velocity difference can be rewritten as

$$U^{(1)} - U^{*(1)} = \nabla_h \phi^{(1)} \tag{41}$$

By taking divergence over Eq. (41), we obtain the Poisson equation for the first-step potential function,

$$\nabla_h^2 \phi^{(1)} = D_h(U^{(1)}) - D_h(U^{*(1)}) \tag{42}$$

From Eq. (30), the first-step velocity $U^{(1)}$ should satisfy the continuity equation, i.e.,

$$D_h(U^{(1)}) = 0 \tag{43}$$

It follows that the Poisson equation for the first-step potential function can be simplified as

$$\nabla_h^2 \phi^{(1)} = -D_h(U^{*(1)}) \tag{44}$$

Since the first-step intermediate velocity field $U^{*(1)}$ and first-step velocity $U^{(1)}$ satisfy the same boundary conditions as the physical velocity U^{n+1} at time t_{n+1}, it follows from Eq. (41) that the first-step potential function $\phi^{(1)}$ satisfies the Neumann boundary condition

$$\nabla_h \phi^{(1)} = 0 \tag{45}$$

on all the computational boundaries. Equation (44), together with Eq. (45), constitutes the Neumann–Poisson problem for the first-step potential function $\phi^{(1)}$.

In the present DSC-Runge–Kutta scheme, a successive overrelaxation (SOR) method is used to solve the Poisson Eq. (44). The first-step potential function $\phi^{(1)}$ is located at point (i, j) in the staggered grid system, and the Poisson Eq. (44) is, approximated at the point (i, j). Therefore, the SOR expression for Eq. (44) is

$$\phi_{i,j}^{(1)l+1} = \frac{\omega}{\delta_{\Delta x,\sigma}^{(2)}(0) + \delta_{\Delta y,\sigma}^{(2)}(0)} \left[-D_h(U^{*(1)}) - \sum_{k=-W}^{-1} \delta_{\Delta,\sigma}^{(2)}(k\,\Delta x)\phi_{i+k,j}^{(1)l+1} - \sum_{k=1}^{W} \delta_{\Delta,\sigma}^{(2)}(k\,\Delta x)\phi_{i+k,j}^{(1)l} - \sum_{k=-W}^{-1} \delta_{\Delta,\sigma}^{(2)}(k\,\Delta y)\phi_{i,j+k}^{(1)l+1} - \sum_{k=1}^{W} \delta_{\Delta,\sigma}^{(2)}(k\,\Delta y)\phi_{i,j+k}^{(1)l} \right] + (1-\omega)\phi_{i,j}^{(1)l} \tag{46}$$

where superscript l refers to the number of inner iterations. Also, ω is the overrelaxation parameter, which can have a value between 1.0 and 2.0, and can be chosen empirically. The iterative convergence criterion for the computation of Eq. (46) is set to

$$\max |\phi_{i,j}^{(1)l+1} - \phi_{i,j}^{(1)l}| \le \varepsilon \tag{47}$$

where $\varepsilon > 0$ is a given small parameter.

Once the values of $\phi^{(1)}$ and $U^{*(1)}$ are calculated, the first-step velocity $U^{(1)}$ can be evaluated from Eq. (41), i.e.,

$$U^{(1)} = U^{*(1)} + \nabla_h \phi^{(1)} \tag{48}$$

The values of $U^{(1)}$ located outside the computational domain are required for computing the derivatives. Note that in Eq. (48), the values of both velocity components (u and v) are obtained at point (i, j). Therefore, it is necessary to transfer them back into their respective points $(i+\frac{1}{2}, j)$ and $(i, j+\frac{1}{2})$. Meanwhile, in Eqs. (26)–(28), the values of velocity component u need to be computed at the point $(i, j+\frac{1}{2})$. Similarly, the values of velocity component v need to be computed at the point $(i+\frac{1}{2}, j)$. We can use the DSC algorithm to obtain these transformations at the specified grid points, as follows:

$$u_{i,j+\frac{1}{2}} = \sum_{k=-W}^{W} \delta_{\Delta,\sigma}^{(0)} \left[\left(k - \frac{1}{2}\right)\Delta y \right] u_{i,j+k} \qquad u_{i+\frac{1}{2},j} = \sum_{k=-W}^{W} \delta_{\Delta,\sigma}^{(0)} \left[\left(k - \frac{1}{2}\right)\Delta x \right] u_{i+k,j} \tag{49}$$

$$v_{i,j+\frac{1}{2}} = \sum_{k=-W}^{W} \delta_{\Delta,\sigma}^{(0)} \left[\left(k - \frac{1}{2}\right)\Delta y \right] v_{i,j+k} \qquad v_{i+\frac{1}{2},j} = \sum_{k=-W}^{W} \delta_{\Delta,\sigma}^{(0)} \left[\left(k - \frac{1}{2}\right)\Delta x \right] v_{i+k,j} \tag{50}$$

where $\delta_{\Delta,\sigma}^{(0)}$ are the coefficients of the regularized Shannon's delta kernel, given by Eq. (12).

The first-step pressure $p^{(1)}$ can be obtained from Eq. (40):

$$p^{(1)} = p^n - \frac{\phi^{(1)}}{\beta_1 \Delta t} \tag{51}$$

The extension treatment for the values of $p^{(1)}$ located outside is similar to $\phi^{(1)}$. The treatment for the second-step and final-step velocity and pressure fields is similar to that of the first-step procedure.

6. Overall solution scheme. The overall solution scheme can be summarized as follows.

Step 1. (i) Using the known velocity (U^n), pressure (p^n), and temperature (θ^n), the first-step intermediate velocity fields $U^{*(1)}$ is computed according to Eq. (37).

(ii) By making use of $U^{*(1)}$, the first-step potential function $\phi^{(1)}$ is evaluated by employing the SOR, according to Eq. (46). The convergence of this inner iteration is controlled by the parameter ε.

(iii) By using $\phi^{(1)}$ and $U^{*(1)}$, the first-step velocity $U^{(1)}$ is evaluated from Eq. (48).

(iv) By using $\phi^{(1)}$, the first-step pressure $p^{(1)}$ is updated according to Eq. (51).

Step 2. Repeat (i)–(iv) of *Step 1* with $U^{(1)}$ and $p^{(1)}$ obtained in *Step 1* instead of U^n and p^n to compute the second-step intermediate velocity fields $U^{*(2)}$ and the second-step potential function $\phi^{(2)}$. Then, second-step velocity $U^{(2)}$ and pressure $p^{(2)}$ are obtained.

Step 3. Repeat (i)–(iv) in *Step 1* with $U^{(2)}$ and $p^{(2)}$ obtained in *Step 2* instead of $U^{(1)}$ and $p^{(1)}$ to compute the third-step intermediate velocity fields $U^{*(3)}$ and the third-step potential function $\phi^{(3)}$. Then velocity U^{n+1} and the pressure p^{n+1} at time t_{n+1} are evaluated.

Step 4. Using the corrected values of velocity (U^{n+1}) and temperature (θ^n), the value of θ^{n+1} is evaluated by using Eq. (36).

The procedure mentioned above (*Step 1–Step 4*) is repeated (outer iterations) until an overall convergence to a steady state is achieved.

C. Finite-Element Approach

The popular projection method of Chorin [26] was extended to finite-element laminar flow problems by Donea et al. [29]. A modified version of the velocity-correction method was proposed by Ren and Utnes [30]. In the FEM, the equations are multiplied by a weight function before they are integrated over the entire computational domain. This is a distinguishing feature compared to either finite-difference or finite-volume schemes. In the present study, we employ a finite-element-based Galerkin weighted residual formulation to implement the velocity correction algorithm [30]. Here, both spatial and temporal discretizations are rendered second-order-accurate. The details of the finite-element shape functions are available in Segarlind [31]. After obtaining velocity, pressure, and temperature over the domain, requisite parameters of design interest are obtained. Detailed formulation is available in Ren and Utnes [30] and Patnaik et al. [38].

It is essential to confirm that the numerical simulation constitutes a desirable representation of the governing PDEs. In the present finite-element scheme, stability

of the algorithm is governed by the advection-diffusion term in the velocity-prediction phase. Thus, the time step (Δt) is obtained from

$$C < \frac{Pe_c}{(2 + Pe_c)} \tag{52}$$

where C is the Courant number, $C = u\,\Delta t/\Delta x$, and Pe_c is the cell Peclet number, $Pe_c = u\,\Delta x/\nu$. Here, Δt and Δx refer to the minimum allowable time step and smallest spatial interval, respectively.

III. RESULTS AND DISCUSSION

Most of the publications which report successful numerical simulations in CFD, in general, present a wide variety of benchmark problems such as flow over a backward-facing step, lid-driven cavity, buoyancy-driven cavity, flow past a circular or square cylinder, flow over a bundle of tubes, etc. Choosing problems with complex fluid flow geometries and boundary conditions, although it strengthens the claims of robustness of the schemes, reduces the clarity of focus. Against this background, we concentrate only on the problem of a buoyancy-driven cavity and present a focused study. We also bring out some of the wide variations observed in the available literature. Benchmark-quality results are presented by employing the quasi-wavelet-based DSC approach described earlier. Extensive use of FEM simulations further support the present investigations.

A. Convergence Study

The purpose of this subsection is to verify the convergence and establish reliability for the present DSC and FEM solutions. An assessment of the consistency and grid-independent nature of the numerical simulation procedure is, of course, of fundamental importance. Error in a numerical simulation is defined as the difference between exact and approximate solutions. The real size of the error can never be computed, due to the nonavailability of an analytical solution for the present problem. However, it is possible to construct an estimate of the error. Such an estimate provides a reliable picture not only of the size of the error, but also of the rate of convergence for the numerical simulations. A variety of error norms are available for this purpose. In the present study, reduction in incremental error between two successive iterations was taken as the criterion for convergence. Such an error is defined as

$$E_{\text{in}}^{n} = \max |\eta^{n+1} - \eta^{n}| \tag{53}$$

where η refers to the primitive variable of interest, such as velocity, pressure, or temperature. The variation of E_{in}^{n} against time can be regarded as convergence history, and such a plot is given in Figure 2, for both DSC and FEM simulations at $Ra = 10^5$. The profile of the convergence history by DSC is flat after $t = 0.5$, as the simulations are restrained by the inner iterative process for the potential function in Eq. (47). Such a constraint does not exist for FEM calculations. However, it should

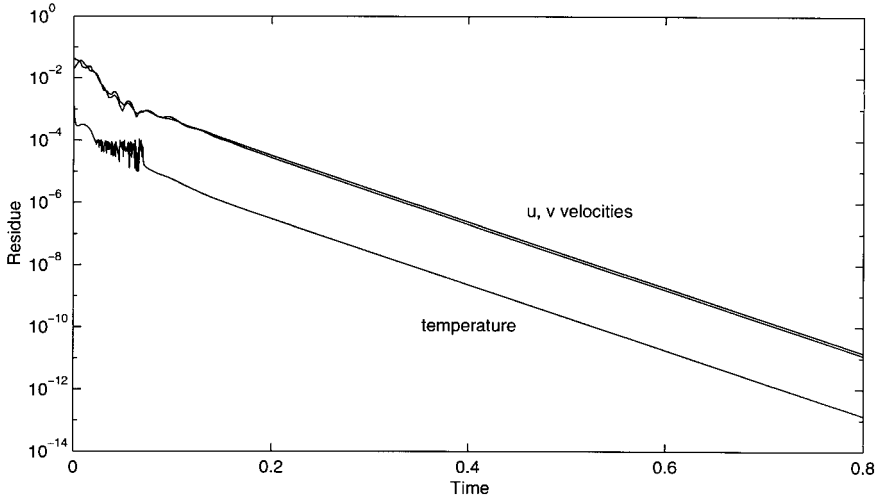

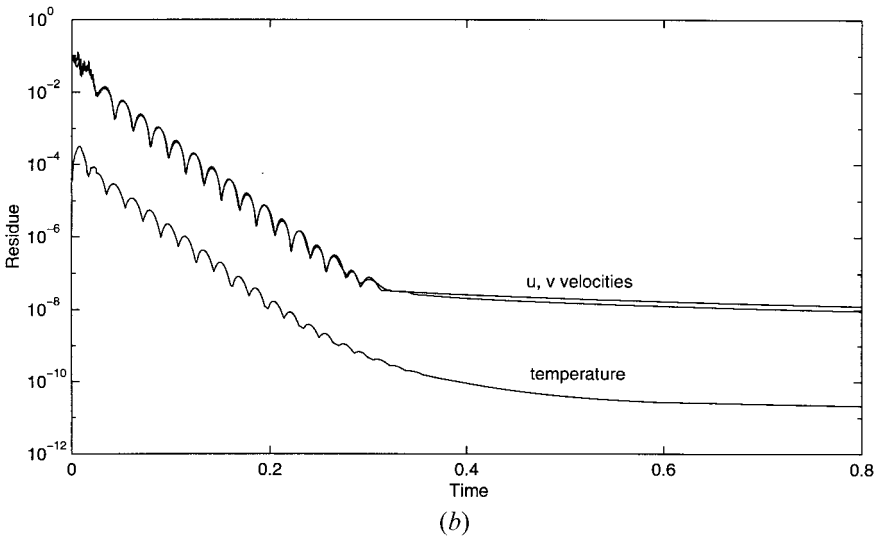

Figure 2. Temporal variation of convergence history for u, v, and θ: (*a*) FEM; (*b*) DSC.

be pointed out that in DSC simulations, much higher accuracy is possible by setting a smaller value for ε and a larger DSC parameter for W. It can be further noticed that the residues of temperature converge faster than the velocity in both DSC and FEM calculations. To ensure a steady-state solution, the following inequality, $E_{\text{in}}^{n} \leq 10^{-8}$, is satisfied in all simulations.

For fluid dynamical simulations, the temporal convergence alone is not enough to ensure the correctness of the solution. The algebraic equations being solved may not be consistent with the physical model. These errors could be due to truncation,

Table 1. Grid sensitivity studies: convergence for vertical velocity (v) and temperature (θ) along the mid-height ($y = 0.5$)

	21×21		41×41		81×81		161×161	
x-Coordinate	v	θ	v	θ	v	θ	v	θ
0.00000	0.00000	1.00000	0.00000	1.00000	0.00000	1.00000	0.00000	1.00000
0.10000	67.66134	0.61325	64.88415	0.60201	63.74017	0.59636	63.25311	0.59351
0.20000	18.84612	0.47001	17.11070	0.47021	16.49249	0.47007	16.22780	0.46987
0.30000	−0.25020	0.48141	−0.52181	0.48306	−0.61296	0.48355	−0.64985	0.48355
0.40000	−1.87755	0.49680	−1.84403	0.49768	−1.83100	0.49787	−1.82631	0.49772
0.50000	−0.00526	0.49974	−0.00005	0.49995	−0.00080	0.49992	−0.00378	0.49968
0.60000	1.86782	0.50273	1.84395	0.50223	1.82940	0.50197	1.81886	0.50165
0.70000	0.23980	0.51827	0.52105	0.51686	0.61041	0.51629	0.63937	0.51583
0.80000	−18.86443	0.52992	−17.11324	0.52975	−16.49663	0.52977	−16.24279	0.52952
0.90000	−67.67705	0.38659	−64.88387	0.39796	−63.73526	0.40351	−63.23259	0.40597
1.00000	0.00000	0.00000	0.00000	0.00000	0.00000	0.00000	0.00000	0.00000

round-off, approximations, interpolation, model constants, etc. Hence, one has to ensure that errors produced in the process of approximation are not magnified during the course of the numerical simulation. There are two systematic ways of error reduction, viz., grid adaptation and mesh refinement. Although the former procedure is dynamic, it also requires a complex and reliable algorithm and could be computationally expensive. The second approach is to choose a series of mesh systems to arrive at a reliable mesh. Choosing a judicious mesh system for the present problem of a buoyancy-driven cavity is obvious, as most of the high-gradient regions are located close to the walls. A series of grid systems (21×21, 41×41, 81×81, 161×161) have been employed to arrive at a grid-independent solution for $\mathrm{Ra} = 10^5$. The data are summarized in Table 1 for velocity and temperature. As can be observed, due to the high accuracy of the DSC approach, even a grid size of 21×21 can produce a reasonable result which compares well with those of other refined grids. Obviously, a grid size of 81×81 is adequate for simulation by the DSC, to ensure consistence and reliability in the present investigations.

B. Velocity Distribution

Initially, the fluid inside the cavity is maintained at the same temperature as that of the cold wall. The fluid picks up heat from the hot wall and loses it to the cold wall. There is no transfer of heat through the horizontal walls (either inside or outside). A wide variety of fluid flow and heat transfer features evolve as a function of the Rayleigh number and their precise simulation is indeed a real challenge to any numerical scheme. To start with, comparison of vertical velocity distribution at the mid-height ($y = 0.5$) as a function of the abscissa is presented in Figure 3*a*, over the Ra range of 10^3 to 10^6, where a grid size of 101×101 was employed. In addition to the numerical simulation by the present DSC and FEM, results from Massarotti et al. [5] are also plotted. Although there is excellent agreement between the present FEM and DSC results, there is a lack of comparison with the predictions of the CBS scheme [5]. The latter has had widely reported success with a variety of problems in

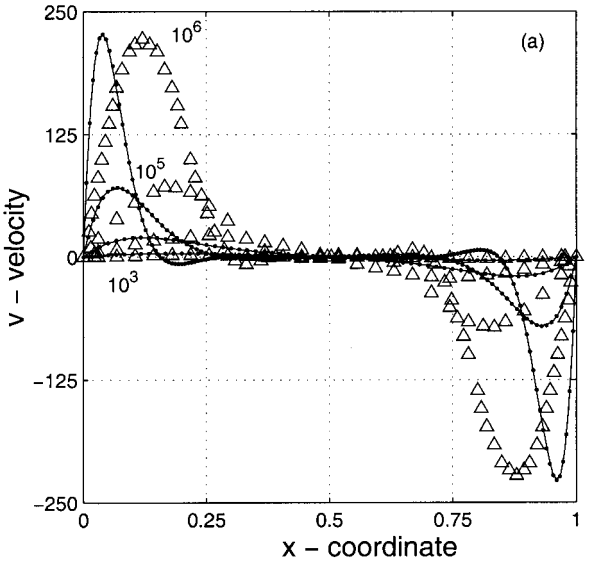

(a)

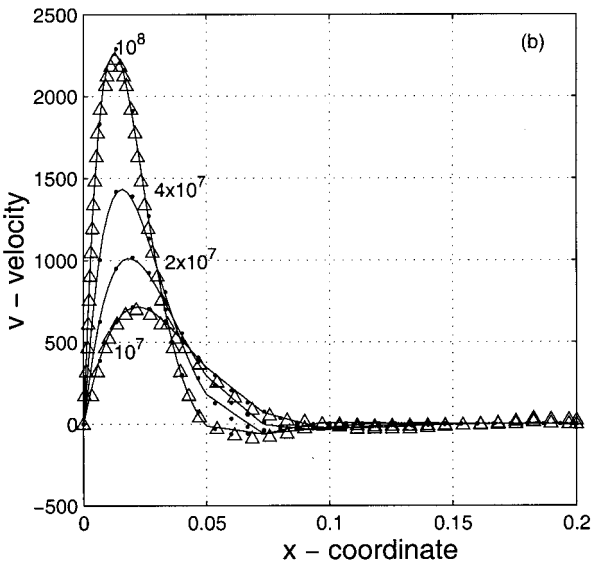

(b)

Figure 3. Comparison of vertical velocity (v) at the mid-height ($y = 0.5$): (*a*) $10^3 \leq \mathrm{Ra} \leq 10^6$, △△△ Massarotti et al. [5]; ·····DSC, ——— FEM; (*b*) $10^7 \leq \mathrm{Ra} \leq 10^8$, △△△ Mayne et al. [10], ·····DSC, ——— FEM.

fluid dynamics [27, 36, 37]. In fact, the vertical velocity distribution has a direct relation to the size of the boundary layer formed on the hot and cold walls. Therefore, it needs to be resolved as accurately as possible. Nevertheless, it should be pointed out that all three completely different numerical simulations yield similar peak values.

The velocity distribution for $10^7 \leq \mathrm{Ra} \leq 10^8$ is plotted in Figure 3*b*. The discretization uses a 301×301 grid for this Ra range to ensure the correctness of the DSC results, although a relatively smaller mesh size also works well. Recent results of Mayne et al. [10] are also compared for $\mathrm{Ra} = 10^7$ and 10^8. There is a good congruence among all the three independent numerical approaches. As the velocity distribution indicates, the boundary layer is more closely confined to the vertical walls with increase in the Rayleigh number. There is a reasonable correspondence between the present DSC and FEM results, even for high Rayleigh numbers. The maximum vertical velocity at the mid-height ($y = 0.5$) and its corresponding x coordinate are presented in Table 2. Such a tabular comparison appears to be popular with other investigators as well. Table 2 also summarizes the maximum values obtained by de Vahl Davis [3], Ramaswamy et al. [8], Massarotti et al. [5], Manzari [6], and the more recent investigations of Mayne et al. [10] with good correspondence among the various schemes. For example, there is a maximum difference of about 6% for $\mathrm{Ra} = 10^6$ between the results of de Vahl Davis [3] and Ramaswamy et al. [8], and all other values fall in between these two investigations. However, such good comparison is not completely encouraging, as Figure 3*a* has indicated that completely noncoincidental velocity distributions can still have the same maximum value. Therefore, we advocate comparison of the entire velocity distribution, both horizontal and vertical velocities at the mid-width and the mid-height, respectively. Variation of horizontal velocity at the mid-width against the ordinate is presented in Figure 4. This plot indicates the direction and intensity of

Table 2. Comparison of maximum vertical velocity (v) at the mid-height ($y = 0.5$)

Ra	Ref. [3]	Ref. [8]	Ref. [5]	Ref. [6]	Ref. [10]	Present study FEM	Present study DSC
10^3	3.679	–	3.692	3.73	3.6962	3.686	3.686
	(0.179)			(0.1827)	(0.1790)	(0.188)	(0.183)
10^4	19.51	19.62	19.63	19.9	19.6177	19.79	19.98
	(0.12)			(0.1246)	(0.1195)	(0.12)	(0.117)
10^5	68.22	68.62	68.85	70.0	68.6920	70.63	70.81
	(0.066)			(0.068)	(0.0665)	(0.072)	(0.070)
10^6	216.75	232.97	221.6	228	220.8331	227.11	227.24
	(0.0387)			(0.039)	(0.0380)	(0.040)	(0.040)
10^7	–	717.04	702.3	698	703.2536	714.48	714.47
				(0.0235)	(0.0215)	(0.022)	(0.021)
2×10^7	–	–	–	–	–	995.33	1017.84
						(0.0156)	(0.02)
4×10^7	–	–	1417	–	–	1435.5	1419.84
						(0.0156)	(0.0133)
10^8	–	–	–	–	2223.4424	2259.08	2290.13
					(0.013)	(0.012)	(0.013)

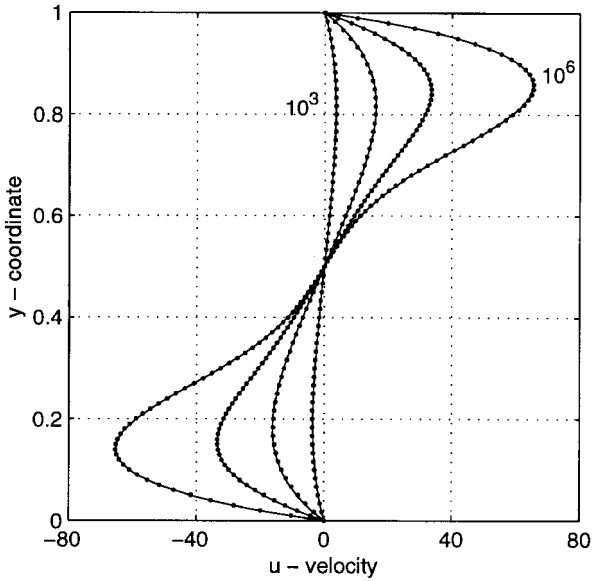

(a)

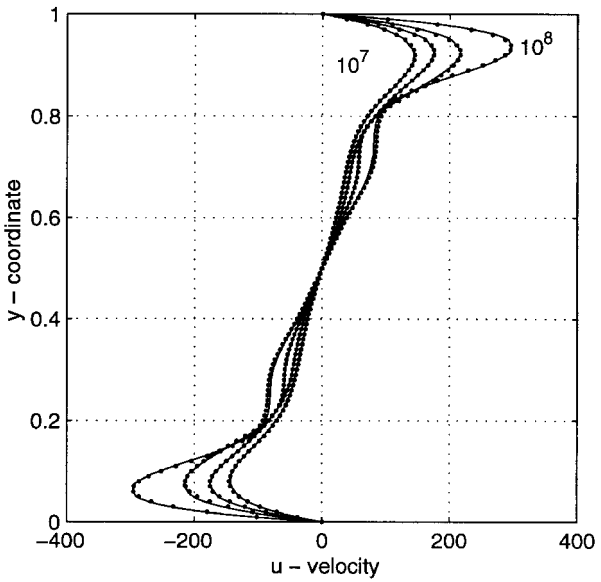

(b)

Figure 4. Variation of horizontal velocity (u) at the mid-width ($x = 0.5$): (a) $10^3 \leq \mathrm{Ra} \leq 10^6$; ($b$) $10^7 \leq \mathrm{Ra} \leq 10^8$; $\cdots$ DSC, ——— FEM.

Table 3. Comparison of maximum horizontal velocity (u) at the mid-width ($x = 0.5$)

Ra	Ref. [3]	Ref. [6]	Ref. [10]	Present study FEM	Present study DSC
10^3	3.634 (0.813)	3.68 (0.817)	3.6493 (0.8125)	3.489 (0.813)	3.6434 (0.8167)
10^4	16.2 (0.823)	16.1 (0.817)	16.1798 (0.8235)	16.122 (0.815)	15.967 (0.8167)
10^5	34.81 (0.855)	34.0 (0.857)	34.7741 (0.8535)	33.39 (0.835)	33.51 (0.85)
10^6	65.33 (0.851)	65.4 (0.875)	64.6912 (0.8460)	65.40 (0.86)	65.55 (0.86)
10^7	–	139.7 (0.919)	145.2666 (0.8845)	143.56 (0.922)	145.06 (0.92)
2×10^7	–	–	–	175.28 (0.93)	175.22 (0.93)
4×10^7	–	–	–	216.85 (0.93)	216.67 (0.92)
10^8	–	–	283.689 (0.9455)	296.71 (0.93)	295.67 (0.94)

fluid motion to be between the left and right zones of the square cavity. Both the DSC and FEM have shown a very good comparison even at $\mathrm{Ra} = 10^8$. Table 3 summarizes maximum horizontal velocities among the values at the mid-width ($x = 0.5$). Also illustrated are the values given in [3], [6], and [10]. A good comparison can be seen among the investigations, particularly between the present DSC and FEM results. However, when maximum values are compared, it is more reasonable to scan the entire domain of the cavity, and not just along the mid-width or mid-height. Therefore, for the purpose of benchmarking, maximum horizontal and vertical velocities and their corresponding coordinate positions are summarized in Table 4. This table should be useful for future comparisons with new computational schemes. It should be particularly noted that the maximum horizontal velocity for $\mathrm{Ra} \geq 10^5$ does not occur along or close to the mid-height, but rather is noticed at a point close to the top left corner of the domain. This aspect further strengthens the need to scan the entire domain of the cavity when obtaining maximum values. As Table 4 shows, there is good correspondence between the DSC and FEM findings. However, there are minor variations in the exact location of the values of this maxima in the domain.

Table 4. Maximum u and v velocities and their corresponding locations over the entire domain

	u-Velocity (x, y position)		v-Velocity (x, y position)	
Ra	FEM	DSC	FEM	DSC
10^3	3.657 (0512, 0.812)	3.648 (0.516, 0.816)	3.692 (0.188, 0.488)	3.69 (0.183, 0.483)
10^4	16.14 (0.489, 0.812)	15.968 (0.5, 0.816)	19.91 (0.119, 0.465)	20.1 (0.1167, 0.467)
10^5	41.88 (0.281, 0.881)	41.82 (0.29, 0.88)	70.81 (0.07, 0.488)	70.83 (0.07, 0.49)
10^6	114.3 (0.164, 0.927)	114.53 (0.173, 0.93)	228.05 (0.037, 0.441)	227.88 (0.04, 0.47)
10^7	339.45 (0.108, 0.963)	339.67 (0.1067, 0.96)	720.54 (0.021, 0.439)	720.43 (0.02, 0.44)
2×10^7	463.58 (0.0796, 0.968)	472.95 (0.093, 0.97)	1020.13 (0.0184, 0.438)	1019.08 (0.02, 0.48)
4×10^7	668.74 (0.075, 0.974)	663.75 (0.08, 0.97)	1446.39 (0.016, 0.438)	1435.36 (0.013, 0.43)
10^8	1055.47 (0.07, 0.978)	1006.26 (0.0667, 0.98)	2291.05 (0.0132, 0.438)	2293.67 (0.0133, 0.48)

C. Natural-Convection Patterns

This subsection analyzes the natural-convection patterns set up by the buoyancy force. The extent of this force is indicated by the Rayleigh number, which in turn dictates both the fluid flow and heat transfer characteristics in the domain. Streamlines, isovelocity contours, and isotherms are plotted in Figure 5, to understand and analyze these wide variety of features. The square-cavity problem with differentially heated vertical walls has two distinct flow patterns: (1) growth of the

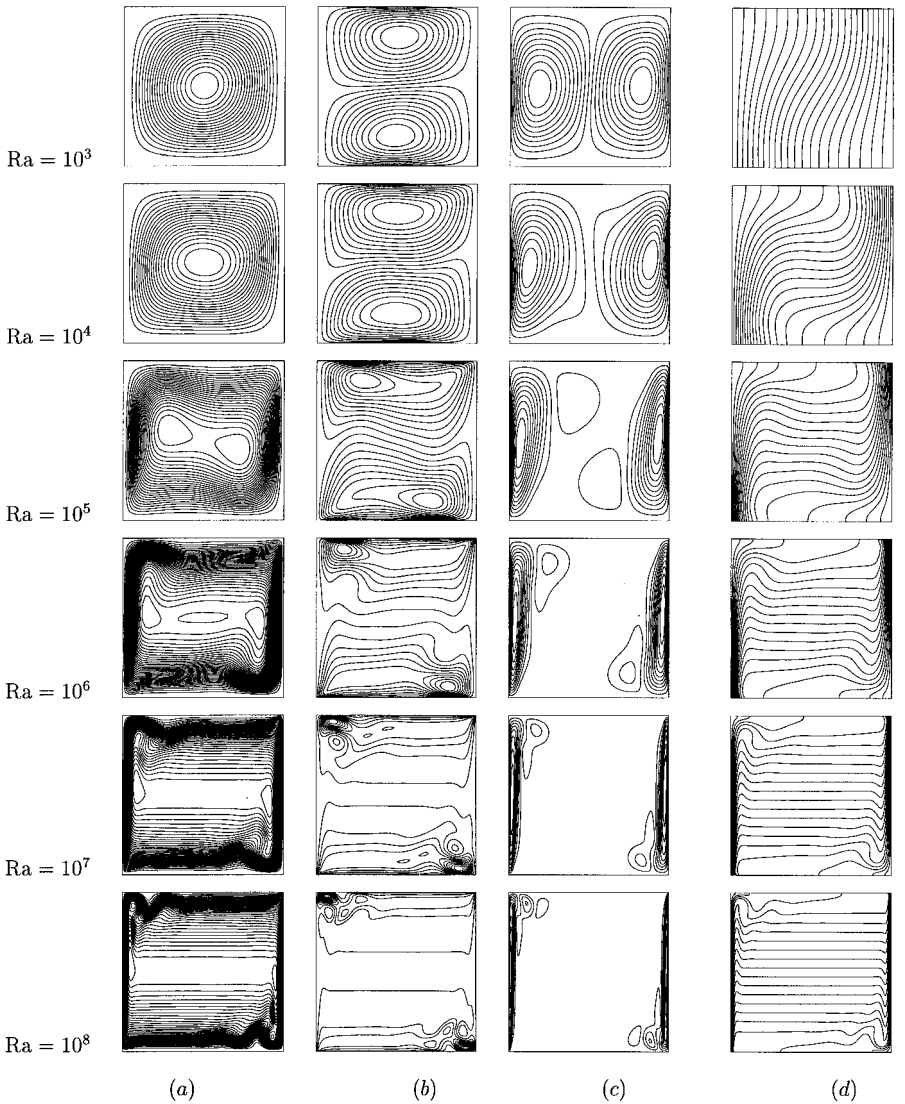

Figure 5. Natural-convection patterns simulated by DSC, $10^3 \leq \mathrm{Ra} \leq 10^8$: (*a*) streamlines; (*b*) iso-*u* contours; (*c*) iso-*v* contours; (*d*) isotherms.

boundary layer along the wall; (2) a recirculating motion in the core region. The latter is prominent in the lower-Ra range, while the former dominates the higher-Ra range. However, both patterns suffice in the medium-Ra range. These features are very well depicted in the streamlines of Figure 5. Only a single circulating eddy persists for $Ra = 10^3$ and 10^4. For $Ra = 10^5$, the inner most zone of the main recirculation splits into two smaller counterrotating eddies in the core region. These two small inner eddies are stretched toward the top left and bottom right corners, retaining the dominance of the main circulation. There exists a saddle point along an imaginary line joining these two inner eddies. With increase in Rayleigh number (10^6), there is a further transformation in the fluid flow patterns, with the inner secondary eddies moving more closer to the hot wall and the cold wall. For still higher values of Ra, they become weaker in strength and are eventually confined to the topmost left and bottommost right corners of the square cavity.

The isovelocity contours in Figure 5 reveal several prominent features. In the u-velocity contours there are two horizontal eddies, one below the other, for $Ra = 10^3$. For higher values of Rayleigh number, these two eddies move closer to the two adiabatic walls. Similarly, two dominant circulations are prominently visible in the vertical isovelocity contours (one each on the left and right zones of the cavity) for $Ra = 10^3$. These two eddies subsequently move closer to the hot wall and the cold wall with an increase in the Rayleigh number. This indeed illustrates that the boundary layer gets thinner as a function of the Rayleigh number. The changes that occur in the isotherms (constant-temperature contours) as a function of the Rayleigh number seems to be more exciting. For $Ra = 10^3$ and below, the contours are nearly vertical and gradually transform into a horizontal grill-like pattern with increase in Ra. Nevertheless, the contours are normal to the horizontal adiabatic walls. This indeed indicates that there is no movement of heat flow through this boundary. In the immediate neighborhood of the hot and cold walls, the contours remain parallel to the isothermal vertical walls. What is particularly fascinating is the existence of a wide range of fluid flow and heat transfer characteristics in such a simple geometry, where the patterns are dictated purely by the force of buoyancy. There is a very good visual comparison for the streamlines, isovelocities, and isotherms, over a wide range of Rayleigh numbers, as they depict similar characteristic fluid flow and heat transfer patterns. In fact, there is complete unanimity in the available literature and visuals of the present simulation. As will also be seen later, such good qualitative comparison of gross features is not adequate and should not be misconstrued.

D. Thermal Distribution

Knowledge of heat transfer coefficient along the hot and cold walls is invaluable to thermal engineers and designers. Nusselt number (Nu) represents the desired nondimensional parameter of interest, which is the ratio of heat convected from the wall to the fluid, to that conducted up to the wall. This can be given by the following relation:

$$\mathrm{Nu}_{\mathrm{local}} = \pm \frac{\partial \theta}{\partial x}\Big|_{\mathrm{wall}} \tag{54}$$

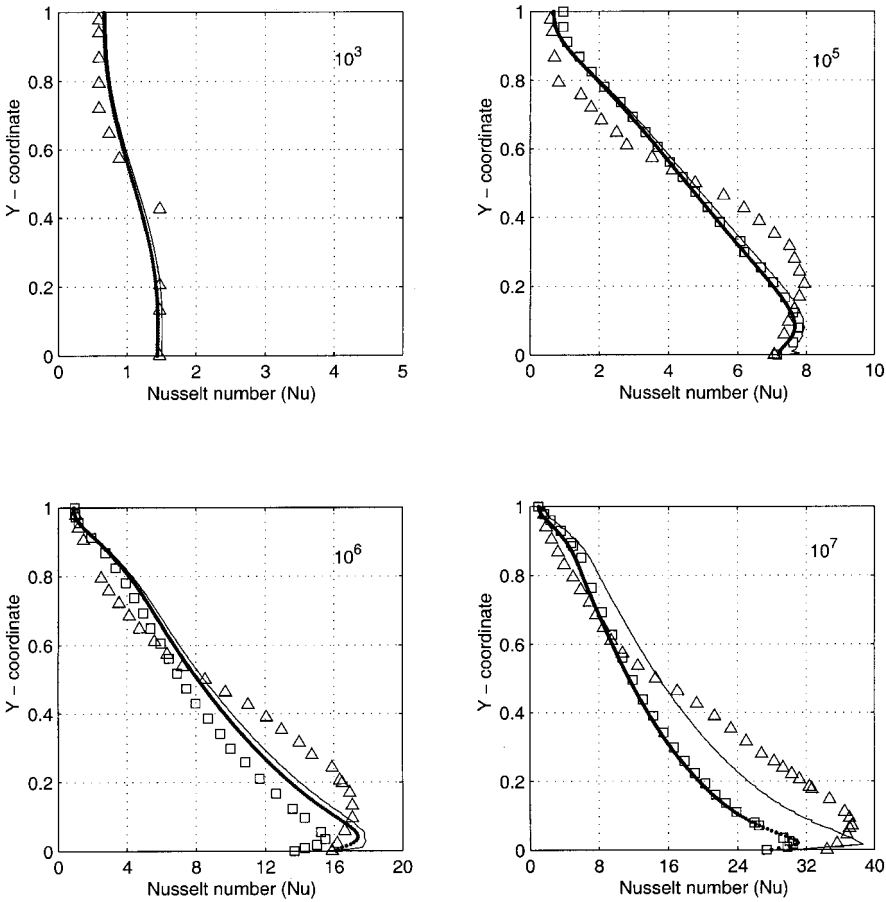

Figure 6. Comparison of local Nusselt number along the hot wall for $10^3 \leq Ra \leq 10^7$: △△△ Massarotti et al. [5], □ □ □ Manzari [6], · · · · DSC, ——— FEM.

In the expression above, a negative sign essentially implies transfer of heat from the wall to the fluid (for the hot wall), while a positive sign means from the fluid to the wall (for the cold wall). Local Nusselt number distribution is compared, in Figure 6, with the results of [5] and [6]. The pattern of distribution in the low-Ra range differs significantly from that in the high-Ra range. In the low-Ra range, the results have good congruence among the investigations. However, in the medium- and high-Ra range, results by the present DSC and those of Manzari [6] show good correspondence. If this good comparison between the two is any indication of the accuracy of these simulations, the present FEM and CBS results overpredict, particularly for $Ra = 10^6$ and above. Nevertheless, this aspect has to be confirmed by other numerical schemes. Even though there exists very good correspondence between the present DSC and FEM results for both vertical and horizontal velocity distributions (Figures 3 and 4), the local Nu variation is significantly different. However, there is a good similarity in the profiles predicted by DSC and FEM simulations. For $Ra = 10^7$, the predictions by Massarotti [5] show a completely different trend

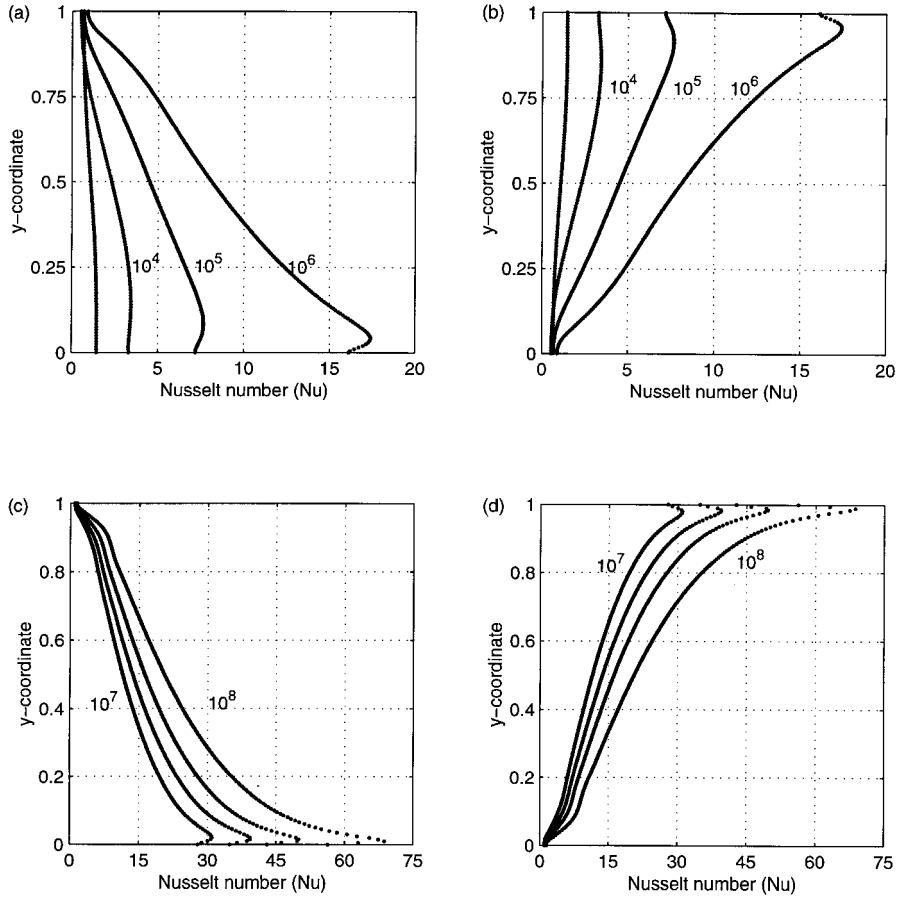

Figure 7. Local Nusselt number variation by DSC simulations: (*a*) hot wall, $10^3 \leq \mathrm{Ra} \leq 10^6$; (*b*) cold wall, $10^3 \leq \mathrm{Ra} \leq 10^6$; (*c*) hot wall, $10^7 \leq \mathrm{Ra} \leq 10^8$; (*d*) cold wall, $10^7 \leq \mathrm{Ra} \leq 10^8$.

compared to the other three simulations, which is evident from Figure 6. Despite the apparent simplicity in the geometry, clarity in the boundary conditions, the phenomenal progress made in computational methods, and the fast-growing number-crunching capability, there is a wide variation among the investigations, even in the prediction of a simple design parameter, viz., the Nusselt number. This lack of unanimity poses a hindrance to the reliable simulation of more complex, industrial-scale fluid flow and heat transfer problems. Further, it also emphasizes the need to resolve this aspect by other independent numerical investigations.

Figure 7 elucidates the local Nusselt number distribution along the hot and cold walls obtained by using the DSC. It is natural to expect an antisymmetric local Nu distribution between the hot and cold walls, as there exists a steady-state asymmetric distribution in the fluid flow and heat transfer patterns. This aspect can be noticed from the figures. There is a greater transfer of heat from the lower bottom of the hot wall to the fluid. Also, the upper top portion of the cold wall picks up

Table 5. Comparison of Nusselt number (Nu) and the corresponding ordinate (max., maximum; min., minimum; Av., average)

Ra	Nu	Ref. [3]	Ref. [8]	Ref. [5]	Ref. [6]	Ref. [10]	Present study FEM	Present study DSC
10^3	Max.	1.50	–	–	1.47	1.5062	1.501	1.444
		(0.092)			(0.109)	(0.08956)	(0.08)	(0.0917)
	Min.	0.692	–	–	0.623	0.6913	0.691	0.665
		(1.0)			(1.0)	(1.0)	(1.0)	(1.0)
	Av.	1.12	–	1.117	1.074	–	1.117	1.073
10^4	Max.	3.53	3.5	–	3.47	3.5305	3.579	3.441
		(0.143)			(0.125)	(0.1426)	(0.13)	(0.1333)
	Min.	0.586	–	–	0.497	0.5850	0.577	0.528
		(1.0)			(1.0)	(1.0)	(1.0)	(1.0)
	Av.	2.243	–	2.243	2.084	–	2.254	2.155
10^5	Max.	7.71	7.71	–	7.71	7.7084	7.945	7.662
		(0.08)			(0.08)	(0.08353)	(0.08)	(0.085)
	Min.	0.729	–	–	0.614	0.7282	0.698	0.678
		(1.0)			(1.0)	(1.0)	(1.0)	(1.0)
	Av.	4.52	–	4.521	4.3	–	4.598	4.352
10^6	Max.	17.92	17.0	–	17.46	17.5308	17.86	17.39
		(0.038)			(0.039)	(0.03768)	(0.03)	(0.04)
	Min.	0.989	–	–	0.716	0.9845	0.9132	0.903
		(1.0)			(1.0)	(1.0)	(1.0)	(1.0)
	Av.	8.8	–	8.806	8.743	–	8.976	8.632
10^7	Max.	–	30.0	–	30.46	41.0247	38.6	31.02
					(0.024)	(0.03899)	(0.015)	(0.02)
	Min.	–	–	–	0.787	1.3799	1.298	0.997
					(1.0)	(1.0)	(1.0)	(1.0)
	Av.	–	–	16.40	13.99	–	16.656	13.86
2×10^7	Max.	–	–	–	–	–	48.84	39.343
							(0.015)	(0.015)
	Min	–	–	–	–	–	1.437	1.106
							(1.0)	(1.0)
	Av.	–	–	–	–	–	19.97	15.46
4×10^7	Max.	–	–	–	–	–	61.69	49.908
							(0.015)	(0.015)
	Min.	–	–	–	–	–	1.59	1.245
							(1.0)	(1.0)
	Av.	–	–	–	23.64	–	23.96	18.597
10^8	Max.	–	–	–	–	91.2095	91.16	68.73
						(0.067)	(0.010)	(0.010)
	Min.	–	–	–	–	2.044	1.766	1.428
						(1.0)	(1.0)	(1.0)
	Av.	–	–	–	–	–	31.486	23.67

more heat from the fluid. This rate of transfer of heat from the wall to the fluid, and vice versa, increases with the Rayleigh number. Local Nu is maximum at a point close to the bottom of the hot wall and minimum at the top. On the cold wall, it is minimum at the bottom and maximum at a point close to the top wall. The locations of these minima, maxima, and averages are summarized in Table 5 together with other investigations. The average Nusselt number, which is a design parameter of interest, is obtained from the following integration:

$$\overline{\mathrm{Nu}} = \int_0^1 \mathrm{Nu}_{\mathrm{local}}\, dy \tag{55}$$

In fact, the uncertainties and complexities grow with increase in the Rayleigh number. Nevertheless, there is good agreement among the investigations up to $\mathrm{Ra} = 10^6$. However, for $\mathrm{Ra} = 10^7$, the average value by Manzari [6] has good correspondence with the present DSC scheme. A careful examination of Table 5 reveals that there is a good correspondence in the prediction of average Nusselt number values among various numerical schemes. However, there are significant discrepancies in the literature in the prediction of local Nu distribution. Therefore, we advocate exercising caution when comparing average Nusselt number values. The area integration under two completely different local Nusselt number distributions can still yield the same average value. This indeed implies that correct values could be obtained for wrong reasons. The numerical fluid flow analyst should be particularly wary of such possible pitfalls.

In the literature, the usual practice is to compare either the average or local Nusselt number values. However, Nusselt number being the first partial derivative of temperature, it is more reasonable to present the latter. Further, the accuracy of the Nusselt number is limited by the approximation of derivatives. To this end, the temperature variation at the mid-height, against the abscissa, in a region close to the hot wall, is presented in Figure 8. Recent results of Mayne et al. [10] compare well with the present DSC and FEM simulations.

IV. CONCLUSIONS

The present study has introduced a high-accuracy quasi-wavelet-based discrete singular convolution (DSC) for the numerical simulation of coupled convective heat transfer problems. A standard finite-element-based Galerkin weighted residual formulation is also implemented with a view to supplement some of the key aspects of the present investigation. Both approaches solve the Navier-Stokes and energy equations by fractional step-based methods. A focused study on the problem of a buoyancy-driven cavity is presented. Benchmark-quality data are generated by using the DSC scheme. A very high level of accuracy, which could be achieved for the Taylor problem [18], is a great asset to surmize its reliability for the driven-cavity problem. A comparative study of the results obtained from a number of other computational schemes is also presented. Some discrepancies have been observed in the literature, and predictions by both the FEM and DSC are presented. Numerical issues such as consistency, convergence, and stability have been addressed. Some specific conclusions are as follows.

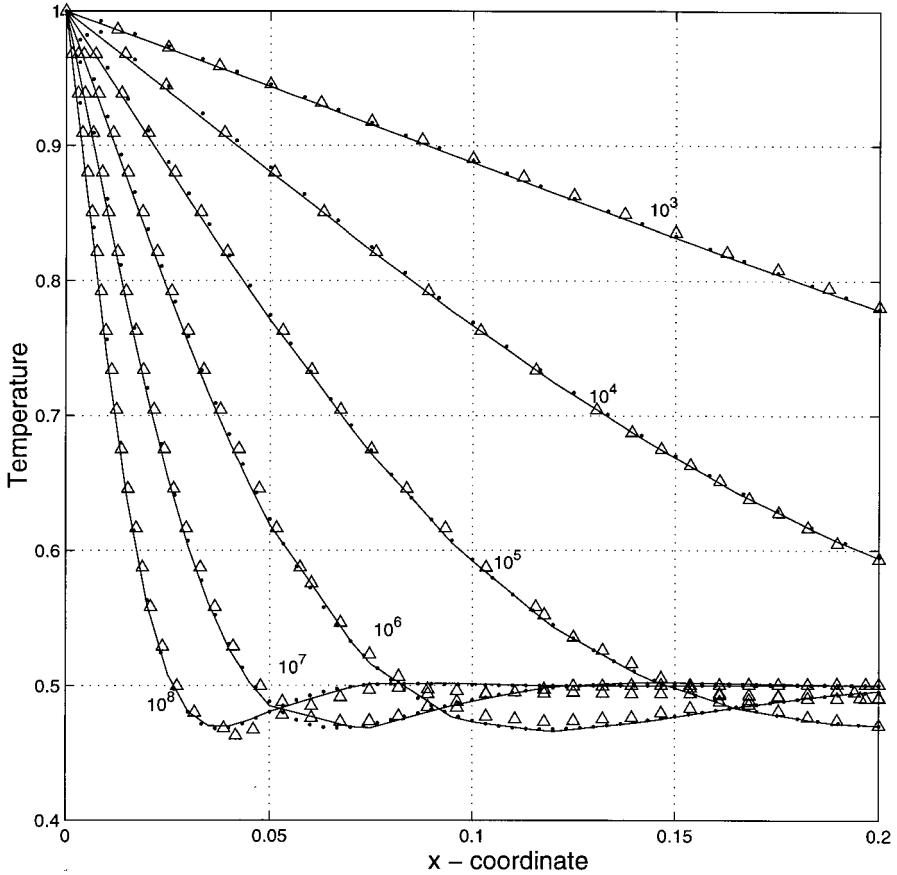

Figure 8. Variation of temperature at the mid-height ($y = 0.5$): △△△ Mayne et al. [10], ····· DSC, ——— FEM.

- Numerical simulation of a buoyancy-driven cavity is extended to the entire laminar natural-convection range $10^3 \leq \mathrm{Ra} \leq 10^8$, while the earlier benchmark data of de Vahl Davis [3] was confined to the range $10^3 \leq \mathrm{Ra} \leq 10^6$.
- All the numerical schemes have produced qualitatively similar natural-convection patterns in terms of streamlines, isovelocities, and isotherms. However, a quantitative comparison of the distribution in terms of primary variables is more crucial.
- Predictions by both the DSC and FEM have shown that good comparison of velocities does not necessarily mean good comparison of the local Nusselt number distribution.
- Numerical schemes should compare the entire velocity and/or local Nusselt number distribution, instead of comparing only the maximum and/or average values, as the latter could lead to erroneous conclusions.
- The lack of good comparison observed in the available literature needs to be resolved further, by other independent numerical schemes.

REFERENCES

1. I. P. Jones, A Comparison Problem for Numerical Methods in Fluid Dynamics: The Double Glazing Problem, in R. W. Lewis and K. Morgan (eds.), *Numerical Methods in Fluids in Thermal Problems*, pp. 338–348, Pineridge Press, Swansea, UK, 1979.
2. D. de Vahl Davis and I. P. Jones, Natural Convection of Air in a Square Cavity: A Comparison Exercise, *Int. J. Numer. Meth. Fluids*, vol. 3, pp. 227–248, 1983.
3. D. de Vahl Davis, Natural Convection of Air in a Square Cavity: A Bench Mark Solution, *Int. J. Numer. Meth. Fluids*, vol. 3, pp. 249–264, 1983.
4. M. Hortmann, M. Peric, and G. Scheuerer, Finite Volume Multi Grid Prediction of Laminar Natural Convection: Benchmark Solutions, *Int. J. Numer. Meth. Fluids*, vol. 11, pp. 189–207, 1990.
5. N. Massarotti, P. Nithiarasu, and O. C. Zienkiewicz, Characteristic-Based-Split (CBS) Algorithm for Incompressible Flow Problems with Heat Transfer, *Int. J. Numer. Meth. Heat Fluid Flow*, vol. 8, pp. 969–990, 1998.
6. M. T. Manzari, An Explicit Finite Element Algorithm for Convective Heat Transfer Problems, *Int. J. Numer. Meth. Heat Fluid Flow*, vol. 9, pp. 860–877, 1999.
7. M. T. Manzari, O. Hassan, K. Morgan, and N. P. Weatherhill, Turbulent Flow Computations on 3D Unstructured Grids, *Finite Elements Anal. Design*, vol. 30, pp. 353–363, 1998.
8. B. Ramaswamy, T. C. Jue, and J. E. Akin, Semi-implicit and Explicit Finite Element Schemes for Coupled Fluid/Thermal Problems, *Int. J. Numer. Meth. Eng.*, vol. 34, pp. 675–696, 1992.
9. C. Shu and H. Xue, Comparison of Two Approaches for Implementing Stream Function Boundary Conditions in DQ Simulation of Natural Convection in a Square Cavity, *Int. J. Heat Fluid Flow*, vol. 19, pp. 59–68, 1998.
10. D. A. Mayne, A. S. Usmani, and M. Crapper, *h*-Adaptive Finite Element Solution of High Rayleigh Number Thermally Driven Cavity Problem, *Int. J. Numer. Meth. Heat Fluid Flow*, vol. 10, pp. 598–615, 2000.
11. F. P. Incropera and D. P. DeWitt, *Fundamentals of Heat and Mass Transfer*, 4th ed., Wiley, New York, 1996.
12. S. Paolucci and D. R. Chenoweth, Transition to Chaos in a Differentially Heated Vertical Cavity, *J. Fluid Mech.*, vol. 201, pp. 379–410, 1989.
13. G. W. Wei, Quasi Wavelets and Quasi Interpolating Wavelets, *Chem. Phys. Lett.*, vol. 296, pp. 215–222, 1998.
14. G. W. Wei, Discrete Singular Convolution for the Solution of the Fokker–Planck Equations, *J. Chem. Phys.*, vol. 110, pp. 8930–8942, 1999.
15. G. W. Wei, A Unified Approach for Solving the Fokker–Planck Equation, *J. Phys. A*, vol. 33, pp. 343–352, 2000.
16. G. W. Wei, Solving Quantum Eigenvalue Problems by Discrete Singular Convolution, *J. Phys. B*, vol. 33, pp. 343–352, 2000.
17. G. W. Wei, A Unified Method for Solving Maxwell's Equation, in *Proc. 1999 Asia-Pacific Microwave Conf.*, Singapore, November 30, 1999, pp. 562–565.
18. G. W. Wei, A New Algorithm for Solving Some Mechanical Problems, *Comput. Meth. Appl. Mech. Eng.*, vol. 190, pp. 2017–2030, 2001.
19. G. W. Wei, Vibration Analysis by Discrete Singular Convolution, *J. Sound Vibration*, vol. 244, pp. 535–553, 2001.
20. G. W. Wei, Discrete Singular Convolution for Beam Analysis, *Eng. Struct.*, vol. 23, pp. 1045–1053, 2001.
21. G. W. Wei, Discrete Singular Convolution Method for the Sine-Gordon Equation, *Physica D*, vol. 137, pp. 247–259, 2000.
22. M. J. Ablowitz, B. M. Herbst, and C. Schober, On Numerical Solution of the Sine-Gordon Equation, *J. Comput. Phys.*, vol. 126, pp. 299–314, 1996.

23. S. Guan, C.-H. Lai, and G. W. Wei, Boundary Controlled Phase Separation in a Circular Domain, *Physica D*, vol. 151, pp. 83–98, 2001.
24. D. C. Wan and G. W. Wei, Numerical Solutions for Unsteady Incompressible Flow Using Discrete Singular Convolution Method, *Int. J. Numer. Meth. Fluids*, revised, 2001.
25. L. W. Qian and G. W. Wei, A Note on Regularized Shannon's Sampling Formulae, submitted, 1999.
26. A. J. Chorin, Numerical Simulation of Navier-Stokes Equations, *Math. Comput.*, vol. 22, pp. 745–762, 1968.
27. R. Codina, M. Vázquez, and O. C. Zienkiewicz, General Algorithm for Compressible and Incompressible Flows, Part III, A Semi-implicit Form, *Int. J. Numer. Meth. Fluids*, vol. 27, pp. 12–32, 1998.
28. R. J. Collins, Band Width Reduction by Automatic Renumbering, *Int. J. Numer. Meth. Eng.*, vol. 6, pp. 345–356, 1973.
29. J. Donea, S. Ginliani, H. Laval, and L. Quartapelle, Finite Element Solution of Unsteady Navier–Stokes Equations by Fractional Step Method, *Comput. Meth. Appl. Mech. Eng.*, vol. 30, pp. 53–73, 1982.
30. G. Ren and T. Utnes, A Finite Element Solution of Time Dependent Incompressible Navier–Stokes Equations Using a Modified Velocity Correction Method, *Int. J. Numer. Meth. Fluids*, vol. 17, pp. 349–364, 1993.
31. L. J. Segarlind, *Applied Finite Element Analysis*, Wiley, New York, 1984.
32. L. Q. Tang and T. H. Tsang, A Least-Squares Finite Element Method for Time Dependent Incompressible Flows with Thermal Convection, *Int. J. Numer. Meth. Fluids*, vol. 17, pp. 271–289, 1993.
33. D. C. Wan and G. W. Wei, Numerical Solutions of Unsteady Incompressible Flows by Discrete Singular Convolution, *J. Comput. Phys.*, revised, 2001.
34. C.-W. Shu and S. Osher, Efficient Implementation of Essentially Non-oscillatory Shock-Capturing Schemes, *J. Comput. Phys.*, vol. 77, pp. 439–471, 1988.
35. J. L. Mead and R. A. Renaut, Optimal Runge–Kutta Methods for First Order Pseudo-spectral Operators, *J. Comput. Phys.*, vol. 152, pp. 404–419, 1999.
36. O. C. Zienkiewicz and R. Codina, A General Algorithm for Compressible and Incompressible Flow, Part I. The Split Characteristic Based Scheme, *Int. J. Numer. Meth. Fluids*, vol. 20, pp. 869–885, 1995.
37. O. C. Zienkiewicz, B. V. K. Satya Sai, K. Morgan, R. Codina, and M. Vaquez, A General Algorithm for Compressible and Incompressible Flows, Part II. Tests on the Explicit Form, *Int. J. Numer. Meth. Fluids*, vol. 20, pp. 887–913, 1995.
38. B. S. V. Patnaik, P. A. A. Narayana, and K. N. Seetharamu, Numerical Simulation of Vortex Shedding Past a Circular Cylinder under the Influence of Buoyancy, *Int. J. Heat Mass Transfer*, vol. 42, pp. 3495–3507, 1999.